

An Aqueous Manganese-Ion Battery with $\text{NaV}_6\text{O}_{15}/\text{C}$ Microrods as a Stable Mn^{2+} Storage Host

Vaiyapuri Soundharajan,^[a] Jun Lee,^[a] Sungjin Kim,^[a] Jung Ho Kim,^[b] Jang-Yeon Hwang,^{*[a, c]} and Jaekook Kim^{*[a]}

Manganese-ion batteries (MIBs) involving aqueous electrolytes are regarded as next-generation energy-storage systems for utilization in safe and non-flammable, grid-scale energy-storing appliances. For practical application, it is very important to establish a stable cathode with a high capacity and stable cycle life. In this respect, vanadium-based layered oxides have been well demonstrated as suitable cathodes for aqueous-electrolyte-based batteries due to their high theoretical capacity and adequate working voltage. However, the dissolution of vana-

dium in the aqueous electrolyte directly affects the cycle life of the vanadium-based layered oxides. In the present study, a carbon-coating approach is established to boost the rate capability and cycling stability of the $\text{NaV}_6\text{O}_{15}$ (NVO) cathode. When employed as a cathode for MIBs, the carbon-coated $\text{NaV}_6\text{O}_{15}$ (NVO/C) supplies a stable recoverable capacity of 149 mAh g^{-1} at 0.4 A g^{-1} after the 1600 consecutive cycles with 88% capacity retention, along with a rapid Mn^{2+} storage ability of 6000 cycles at 3.0 A g^{-1} with 74% capacity retention.

Introduction

The simplicity in usage, energy efficiency, and reusability upsurges consumer usage and increases the demand for affordable rechargeable batteries in the global market.^[1–4] Moreover, the comprehensive research activities on rechargeable batteries from energy experts also mainly focused on consumer and environmental demands.^[5–8] The potential explosion risk and supply chain shortage associated with the commonly used lithium-ion battery (LIB), committed energy researchers to find the best alternate rechargeable batteries. Accordingly, energy experts have successfully registered the formulation of rechargeable batteries using vastly available, economical, and lightweight materials such as aluminum, zinc, and manganese.^[3,4,9–13] Among these, manganese-ion batteries (MIBs), involving high-capacity and low-cost manganese resources have been recent arrival and are regarded as potential alternatives to LIBs for grid-scale applications.^[13]

The cathode is the key component in defining the electrochemical operation of the MIBs,^[14] with reasonable migration

routes and better structural stability being essential aspects of the material formulation due to the large ionic radius of Mn^{2+} (0.83 \AA) relative to that of Zn^{2+} (0.74 \AA).^[13,15] Consequently, vanadium-based layered oxides have drawn huge appeal as cathode materials for MIBs, due to advantageous electrochemical properties such as a high running capacity of ~ 280 – 350 mAh g^{-1} and a high operating voltage of 1–1.3 V based on the $\text{Mn}^{2+}/\text{H}^+$ insertion/deinsertion mechanism.^[14] However, due to the use of aqueous electrolytes, the vanadium-based layered oxides have suffered from various obstacles^[16,17] including poor electrical conductivity and vanadium dissolution, which directly impacts the cycling stability.^[18–20] Hence, addressing these issues surrounding vanadium-based layered oxides is essential.^[21,22] In this respect, surface enhancement practices are demonstrated as a feasible solution to address the interfacial issues of vanadium based layered cathodes in aqueous electrolytes. Carbon coating is an economically viable and industrially established technique for preventing the direct interaction of the cathode with the electrolyte and it is adopted in this study.^[23,24]

Sodium vanadium bronze $\text{NaV}_6\text{O}_{15}$ (NVO) is a well-known layered type electrode material from the vanadium family, which is demonstrated to host both monovalent and divalent charge carriers.^[25,26] In specific, the NVO with unique structural arrangements built by V_4O_{12} layers pillared with pre-intercalated Na^+ ions determined to alleviate the charge density of the incoming alien ions.^[9,26] Combined with the distinctive structural behavior and pillaring effects NVO has been applied to deliver a high Zn^{2+} storage capacity of $\sim 420 \text{ mAh g}^{-1}$ in zinc-ion batteries (ZIBs) and might also prove useful as an Mn^{2+} storage host. Yet, the practical difficulties associated with the intercalation of Mn^{2+} into the NVO host need to be experimentally verified.

In the present study, NVO is first synthesized via a practicable sol-gel technique and then reacted with maleic acid

[a] Dr. V. Soundharajan, J. Lee, Dr. S. Kim, Dr. J.-Y. Hwang, Dr. J. Kim

Department of Materials Science and Engineering

Chonnam National University

Gwangju 500–757 (South Korea)

E-mail: hyy@jnu.ac.kr

jaekook@chonnam.ac.kr

[b] Dr. J. H. Kim

Institute for Superconducting & Electronic Materials (ISEM)

Australian Institute of Innovative Materials (AIIMs)

University of Wollongong

North Wollongong, New South Wales 2500 (Australia)

[c] Dr. J.-Y. Hwang

Department of Energy Engineering

Hanyang University

Seoul 04763 (Republic of Korea)

 Supporting information for this article is available on the WWW under <https://doi.org/10.1002/batt.202200527>

(MA) to obtain carbon-coated $\text{NaV}_6\text{O}_{15}$ (NVO/C). The Mn^{2+} storage properties and electrochemical output of the NVO/C are then studied and compared with those of the uncoated NVO. Finally, it is verified that the conductive carbon layer promotes the rate capability and cycling stability of the NVO/C above that of the pristine NVO.

Results and Discussion

The NVO/C was synthesized from pristine NVO, which was itself prepared via the sol-gel technique, as detailed in the Experimental Section. The PXRD profiles of the NVO and the NVO/C are presented in Figure 1(a), and both are well indexed to the monoclinic type NVO unit (space group A2/m, JCPDS.no 01-077-0146, lattice constants: $a = 10.08 \text{ \AA}$, $b = 3.61 \text{ \AA}$, $c = 15.44 \text{ \AA}$, and $\beta = 109.60^\circ$). The NVO/C XRD patterns exhibit slight amorphous features between 10° and 20° , indicating that the carbon coating is amorphous in nature. The crystal arrangements of the NVO structure are provided in Figure 1(b). The NVO unit exhibits a tunnel-like structure constructed from the vanadium-centered $[\text{VO}_6]$ octahedral units and the $[\text{VO}_5]$ square pyramidal units.^[27] In addition, seven O atoms are aligned with Na ions to build a controlled trigonal prism, where Na utilizes

an occupancy of only 0.5, thereby creating large vacancies for hosting foreign ions in the structure.^[28] This demonstrates that the NVO could be a potential intercalation site for the Mn^{2+} ions.

The SEM image in Figure 1(c) reveals that the NVO/C powder is distributed as a microrod-like structure. Further, the low-resolution TEM image of the single NVO/C product in Figure 1(d) indicates that the width of the micro-rod is $\sim 300 \text{ nm}$, and its length is $\sim 1.0 \mu\text{m}$. In addition, the high-resolution TEM image in Figure S1 reveals that the interplanar spacing of the microrod is 0.29 nm, which corresponds to the (30-4) plane of monoclinic $\text{NaV}_6\text{O}_{15}$, in agreement with the above-mentioned PXRD results. Furthermore, the inset in Figure 1(e) indicates that the NVO micro-rod is coated with a thin layer of carbon ($\sim 3\text{--}5 \text{ nm}$) originating from the maleic acid carbon source. Carbon content in the NVO/C sample is quantified by performing thermogravimetric analysis under air atmosphere from room temperature to 600°C . The amount of carbon in the NVO/C sample was calculated to be 5.8% (Figure S2). In addition, the EDX mapping images of the NVO/C microrods in Figure 1(f) demonstrates the uniform distributions of the elements Na, V, O, and C.

The electrochemical Mn^{2+} storage properties of the NVO/C and NVO electrodes are revealed by the second charge/

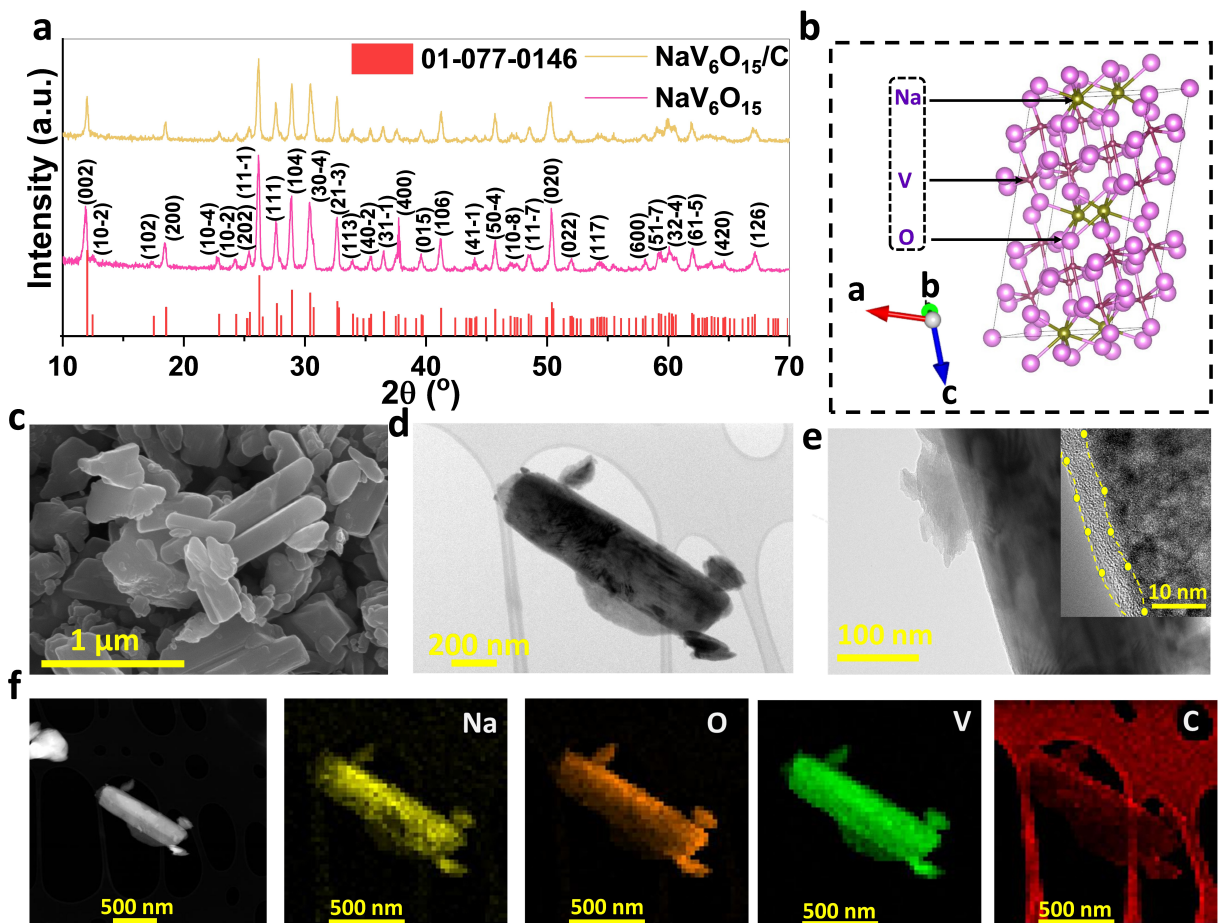


Figure 1. a) PXRD pattern of the NVO/C, b) crystal structure of $\text{NaV}_6\text{O}_{15}$, c) SEM image of NVO/C, d) TEM image of NVO/C, e) high-resolution TEM image with carbon coating (inset), f) Elemental mapping results for the Na, O, V, and C.

discharge cycles in Figure 2(a), where the materials deliver efficient discharge capacities of 238 and 200.6 mAh g⁻¹, respectively. The coulombic efficiency loss in the NVO/C could be associated with the irreversible Mn²⁺ (de)adsorption on the conductive carbon as well as the in-situ formation of electrolyte by-product, i.e., $MnClO_4 \cdot xH_2O \cdot n(OH)$, formation (discussed in the following Section, Figure S3a). Thus, the irreversibility associated with the carbon-coated sample could be correlated with the irreversible Mn interaction with the carbon layer. To understand this assumption, we have compared the electrochemical Zn²⁺ storage properties in the 3 M Zn(ClO₄)₂ electrolyte in the same working voltage (Figure S3a). It can be clearly witnessed that the capacity loss (14%) associated with Zn²⁺ ions is less than the Mn²⁺ ions (34%). This clearly validates that the Mn²⁺ interfacial reaction associated with the carbon-coated contributes to the initial capacity loss for the NVO/C sample. It is well-known that the carbon-coated sample has large interfacial sites, which could induce the additional adsorption/desorption of charge carriers. To understand the impact of conductive carbon on the capacity output, super P carbon is used as a control cathode. The galvanostatic outcome of the super P as the control cathode after 1st discharge cycle exhibits a sloping profile and supplied 10 mAh g⁻¹ (Figure S3b). However, in the consequent charge profile, the insertion behavior is not evident, whereas super P carbon possessed capacitive behavior and supplies increased capacity (70 mAh g⁻¹) as well voltage output via adsorption and desorption of Mn²⁺ and

ClO₄²⁻. Also, the galvanostatic outcome of the super P and NVO/C cathode is compared in (Figure S3c) and it can be clearly seen that the capacity and voltage output of the NVO/C cathode mainly resulted from the NVO/C when used as a primary cathode. Yet, the carbon material can contribute to the capacity output of the NVO/C system to a certain extent via capacitive adsorption properties.

The flatness of each charge/discharge profile is associated with the presence of typical multi-electron V^{5+/4+/3+} redox pairs arising from the insertion and deinsertion of Mn²⁺ ions in the layered structure.^[14,29,30] The rate capabilities of the two electrodes are shown in Figure 2(b), where the manganese loading capacity of the NVO/C electrode is seen to be substantially superior to that of the NVO electrode in the measured range. This might be attributed to the coating of the NVO with high-conductivity carbon in the NVO/C electrode. In detail, the NVO/C electrode exhibits average rate capacities of 252.4, 177.3, 160.5, 147.4, 134.4, 102.6, 88.5, 79, 71.1, and 65 mAh g⁻¹ at current densities of 0.1, 0.2, 0.3, 0.4, 0.5, 1.0, 1.5, 2.0, 2.5, and 3.0 A g⁻¹, respectively. A stable reversible capacity is recovered at 165 mAh g⁻¹ when the current density is reset to 0.3 A g⁻¹. This compares to values of 185.2, 160.9, 147.2, 134.3, 124, 91.1, 74, 64, and 57.4 mAh g⁻¹, respectively, for the bare NVO. The voltage vs. specific capacity curves of NVO/C is provided in Figure S3(d) of the Supplementary Material. The cycle life stability of the NVO/C and NVO cathode at a moderate current density of 0.4 A g⁻¹ is compared in Figure 2(c). The result

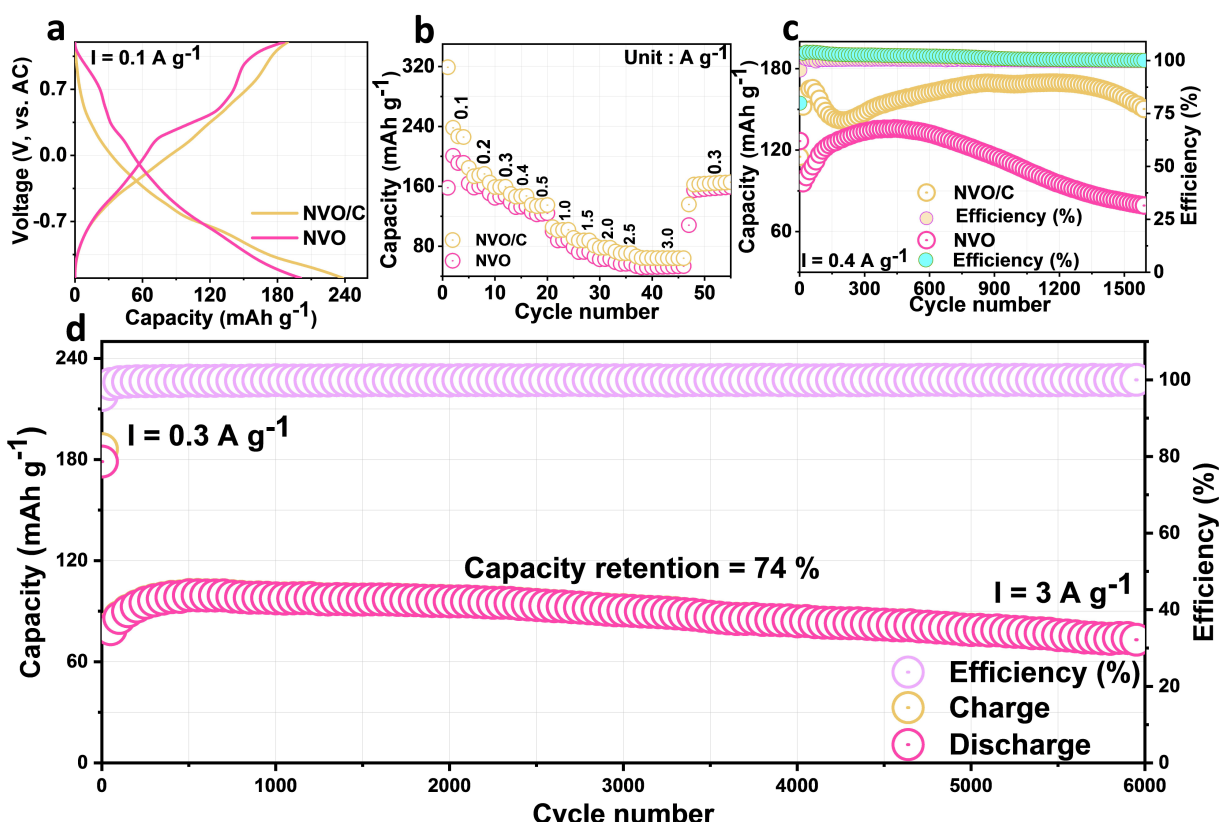


Figure 2. a) Comparison of galvanostatic charge/discharge profiles for NVO and NVO/C cathodes at 0.1 A g⁻¹, b) rate performance evaluation for NVO and NVO/C cathodes, c) cycle life curve for NVO and NVO/C cathodes at 0.4 A g⁻¹, and d) cycle life curve for NVO/C at 3 A g⁻¹.

validates that the carbon coating significantly enhances the life cycle output of the NVO/C sample. After delivering a low initial capacity of 115 mAh g^{-1} , the NVO/C electrode undergoes an activation process to achieve a maximum activation capacity of 169 mAh g^{-1} at the end of the 1200th cycle. Subsequently, the NVO/C cell experiences a slight drop in capacity, and the capacity stabilizes at 149 mAh g^{-1} at the end of the 1600th cycle.

In specific, the reversible capacity (149 mAh g^{-1}) supplied by the carbon coated NVO/C cathode after the 1600 cycle is considerably higher than the reversible capacity (80 mAh g^{-1}) of the carbon free NVO cathode. In specific, the capacity retention output of the NVO/C cathode exhibits 88% of the maximum capacity while that for the NVO cathode is only 59% of the maximum capacity indicating that the NVO/C electrode exhibits a creditable cycling lifetime. Further, the voltage output remains in the redox region throughout the cycling process (Figure S3e), thereby establishing the good structural stability of the NVO/C electrode. When the NVO/C electrode is allowed to stabilize by operation at a low current density of 0.3 A g^{-1} for 3 cycles, and then subjected to a high current density of 3.0 A g^{-1} the results are shown in Figure 2(d) are obtained. Here, the NVO/C electrode exhibits an outstanding cycle life, with a steady reversible capacity of 73 mAh g^{-1} even after 6000 uninterrupted cycles of rapid Mn^{2+} insertion/deinsertion. In detail, the NVO/C electrode initially exhibits a low capacity of 60 mAh g^{-1} when the current density is increased from 0.3 to 3.0 A g^{-1} . However, an activation process eventually occurs, and the cathode achieves an increased discharge capacity of 99 mAh g^{-1} after the 455th cycle. With further cycling, the electrode stabilizes and supplies a persistent discharge capacity of 73 mAh g^{-1} after 6000 cycles with 74% capacity retention. This demonstrates that the NVO/C electrode can provide instant manganese-ion storage properties. Moreover, the identical voltage profiles obtained after multiple charge/discharge processes in Figure S3(f) further demonstrates that the NVO/C framework is preserved throughout the entire cycling process. From the ex situ XRD analysis, it can be witnessed that the crystalline phase of the NVO/C framework after the long cycling is associated with additional peaks (Figure S4). In specific, the additional peak is grown due to the electrolyte salt precipitation reaction, which will be discussed in the following section.

The Mn^{2+} storage kinetics of the NVO/C electrode are revealed by the CV results in Figure 3(a), where the oxidation and reduction curves are enlarged at increased scan rates due to the sustained polarization.^[31] The electrochemical kinetics can be quantified from the linear slope of the log-log curve of peak current (i) against sweep rate (v),^[32] i.e.:

$$i = av^b \quad (1)$$

where a and b are constants, whose value depends on the mechanism. Specifically, previous studies have shown that a b value of 0.5 indicates a diffusion-related mechanism, whereas a b value of 1.0 indicates a capacitive-related process.^[33] In the case of the NCO/C cathode, peaks 1, 2, 3, and 4 in the log-log-

curve has b values of approximately 0.89, 0.54, 0.83, and 0.60, respectively (Figure 3b), thereby signifying that the Mn^{2+} storage kinetics involves a combination of diffusion-related and capacitive processes.

The qualitative analysis of the diffusion (k_1v) and capacitive ($k_2v^{1/2}$) influences at a given potential can be calculated from the following equations:^[34]

$$i(V) = k_1v + k_2v^{1/2} \quad (2)$$

and

$$i(V)/v^{1/2} = k_1v + k_2 \quad (3)$$

Upon calculating the square root of the scan-rate dependence of the current, the parameters k_1 and k_2 can be established from the slope and y-axis intercept.^[35] The k_1 and k_2 values can also be determined from the particular anodic/cathodic scan voltages.^[36,37] After performing the calculation for the entire potential range, the capacitive-induced output (the highlighted zone in Figure 3c) is assessed and plotted at 0.2 mV s^{-1} , for reference. The assessed capacitive contributions at various scan rates are compared in the histogram in Figure 3(d). Thus, the highlighted zone has total capacitive storage outputs of 21%, 30.4%, 31.6%, 36.2%, and 38.5% at scan rates of 0.2, 0.3, 0.4, 0.5, and 0.6 mV s^{-1} , respectively.

The favorable diffusion kinetics of the NVO/C cathode are confirmed by the GITT results in Figure 3(e). The diffusion coefficient of Mn^{2+} ions during the insertion/deinsertion process can be calculated from Fick's second law:^[38-40]

$$D_{\text{Mn}} = 4/\pi\tau(m_B V_M/M_w A)_2(\Delta E_s/\Delta E_t) \quad (4)$$

where τ is the time for a specific galvanostatic current, m_B , V_M , and M_w are, respectively, the mass, molar volume, and molecular weight of the NVO, A is the specific area of the cathode, and ΔE_s and ΔE_t are, respectively, the pseudo-equilibrium voltage and change in the cell voltage E throughout the current pulse.^[41] The profile of the single GITT curve for the 1st discharge process specified with τ , ΔE_s and ΔE_t are provided in Figure S5, for reference. As shown in Figure 3(f and g), the NVO/C cathode exhibits suitable diffusion coefficient outputs during both the discharge (1.2×10^{-9}) and charge (3.29×10^{-9}) processes, thereby confirming the reasonable migration kinetics as that of divalent charge carriers. Diffusion coefficient outputs of the NVO/C cathode are comparable to the ZIBs. The diffusion behaviour is mainly associated with the ideal path of the diffusion channel, electronic conductivity, and the shape of the electrode particles.^[42,43] In this regard, the higher diffusion coefficient output of the NVO/C is contributed by the electronic conductivity improvement via carbon coating as well as the Mn^{2+} diffusion channel associated with the Microrod structure.

The Mn^{2+} storage mechanism of the NVO/C is further revealed by the ex-situ XRD and XPS results in Figure 4. Before the electrochemical process, the cathode exhibits the monoclinic phase (Figure 4a-c). When the cathode is discharged to

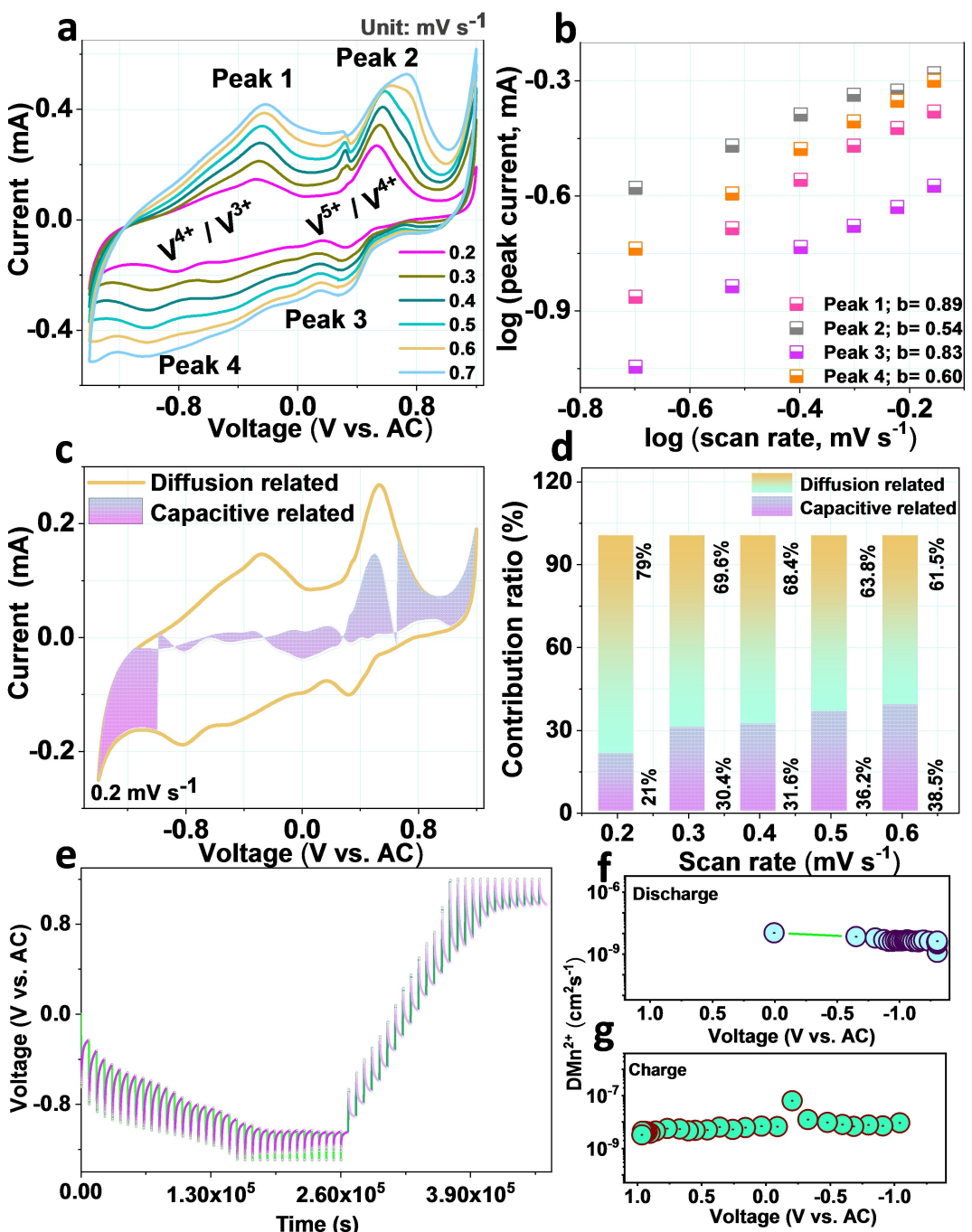


Figure 3. a) CV curves of NVO/C at multiple scan rates. b) Linear relation between $\log(i)$ and $\log(v)$. c) Capacitive contributions at 0.2 mV s^{-1} scan rate. d) Capacitive-diffusion contribution at different scan rates. e) Discharge-charge GITT profiles at a current density of 0.2 A g^{-1} . Mn²⁺ diffusion coefficients of NVO/C at f) discharge and g) charge.

-1.3 V, however, the (002), (11-1), and (600) XRD reflections of the NVO/C exhibit a shift towards a higher angle, thereby indicating that these planes have experienced a reduction in interlayer spacing.^[44] Conversely, the (10-8) reflection has moved to a lower angle, thereby demonstrating that the (10-8) plane has experienced an increase in interlayer spacing.^[37] Ex situ SEM studies after the 1st discharge process are performed to understand the insertion of Mn²⁺ ions, where the microrod morphology of NVO/C is retained (Figure S6a). Moreover, the

SEM/EDS analysis of the microrods revealed Mn composition along with the Na, V, and O during the discharge process, indicating the insertion of Mn²⁺ into the NVO/C microrods (Figure S6b and Table S1). Further, the appearance of two new peaks at 22° and 45.4° implies the formation of inherent parasitic reactions, i.e., the precipitation of $\text{MnClO}_4 \cdot x\text{H}_2\text{O} \cdot n(\text{OH})_y$, originating from the electrolyte. When the cathode is charged to +1.2 V, all the reflections return to their original positions, thereby indicating the recovery of the layered structure and

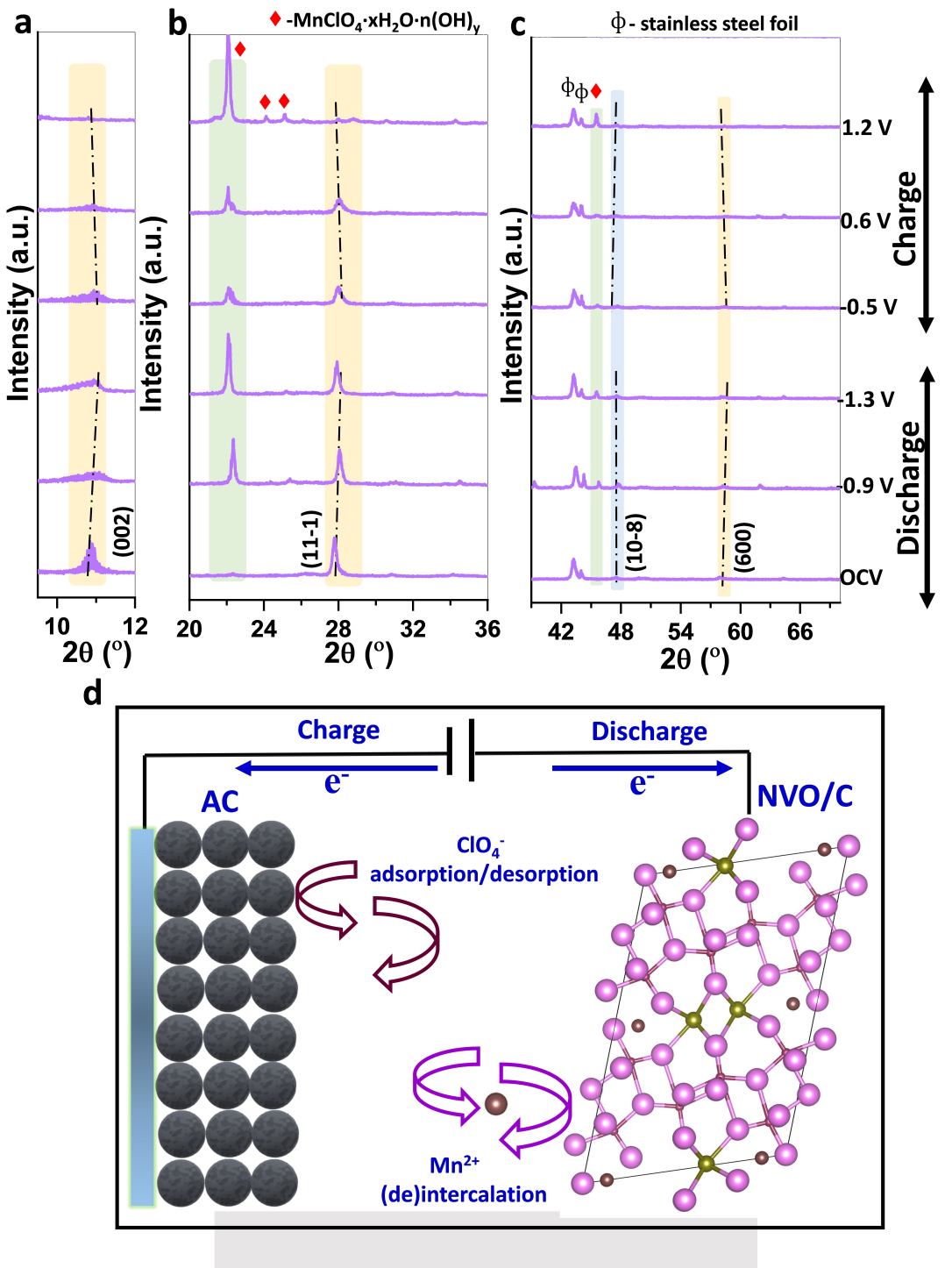


Figure 4. Ex-situ XRD profiles of NVO/C within selected angles a) 9°–12°, b) 20°–36°, c) 41°–67°, and d) schematic illustration of electrochemical Mn²⁺ storage properties of NVO/C.

supporting the hypothesis of Mn²⁺ ion insertion and deinsertion between the NVO/C layers. It must be noted that the $\text{MnClO}_4 \cdot x\text{H}_2\text{O} \cdot n(\text{OH})_y$ was absent in the pristine cathode and retained during the cycling process. The role of the parasitic reaction in the cycling stability of the MIBs will be a subject for future research. Based on the electrochemical and ex-situ XRD investigations, the Mn²⁺ storage properties of the NVO/C

cathode are schematically illustrated in Figure 4(d). The galvanostatic testing studies showed that NVO/C cathode can host a maximum of 3.39 moles of Mn²⁺ ions at 0.1 A g⁻¹, accordingly the electrochemical reaction process can be depicted as $\text{NaV}_6\text{O}_{15} \leftrightarrow \text{Mn}_x\text{NaV}_6\text{O}_{15}$ ($x \geq 3.39$). The ex-situ XPS profile in Figure 5(a) exhibits a V 2p_{3/2} peak located at 517.2 eV, thereby indicating the presence of the V⁵⁺ state of NVO in the

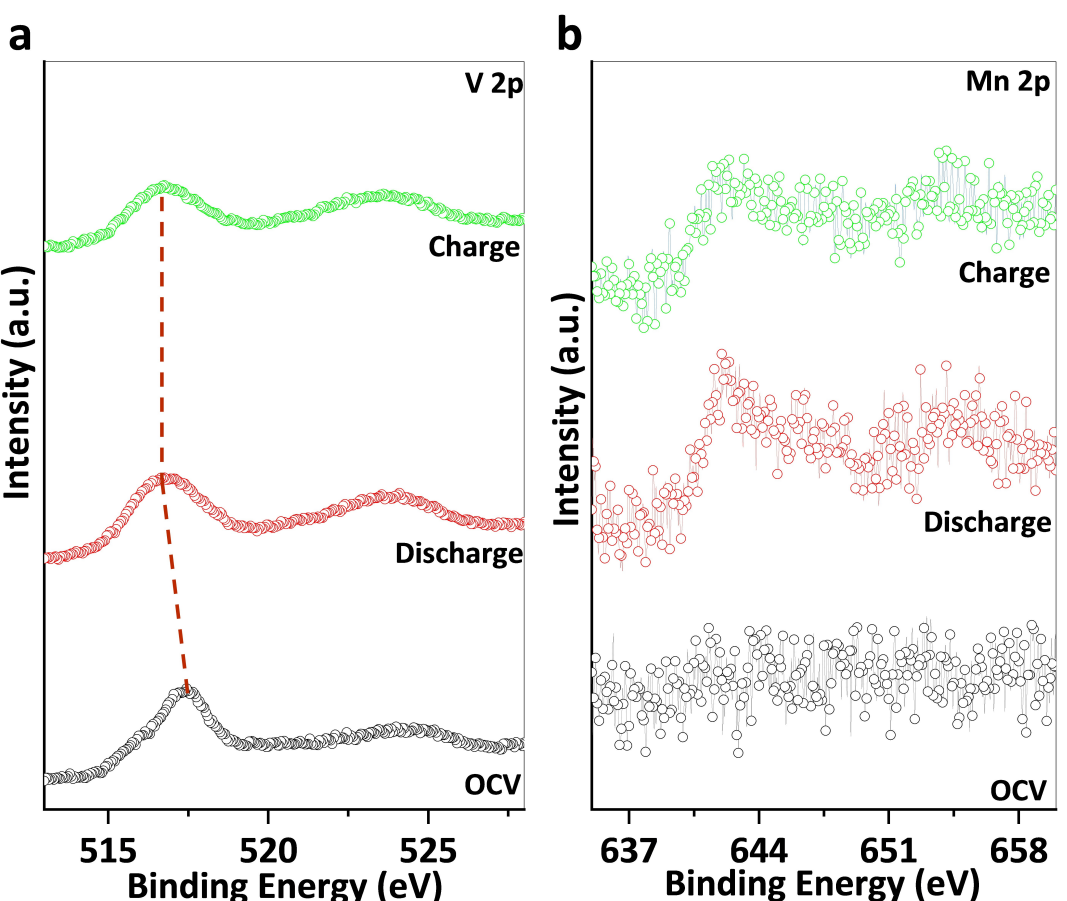


Figure 5. Ex-situ XPS output of the NVO/C cathode after 1st charge and discharge cycles for a) V 2p and b) Mn 2p.

pristine cathode.^[27] After discharging to -1.3 V, however, the V 2p_{3/2} peak is shifted to the lower binding energy of 516.3 eV, thereby indicating the reduction of the V⁵⁺ state to the V³⁺ state and confirming the involvement of multiple redox couples in vanadium charge transfer during the Mn²⁺ insertion process. When the electrode is charged to $+1.2$ V, the V 2p_{3/2} peak is largely restored to its original binding energy, thereby indicating a change in the vanadium oxidation state. Thus, the Mn²⁺ insertion/deinsertion process primarily involves multi-electron redox changes in the vanadium species in the NVO unit. Moreover, while Mn 2p signals are not evident in the pristine cathode (Figure 5b), an intense Mn 2p_{3/2} peak emerges at 642.5 eV in the discharged cathode, thereby confirming both the Mn²⁺ insertion and MnClO₄·xH₂O·n(OH)_y formation in the NVO/C framework. Notably, the Mn 2p_{3/2} peak is still present, albeit with decreased intensity, in the charged cathode, thereby confirming the presence of some remaining MnClO₄·xH₂O·n(OH)_y in the NVO/C cathode.

The findings reveal that the carbon coating enhanced the rate performance and cycle life stability of the NVO/C cathode. In specific, the conductive carbon coating acts as a buffer layer that limits the direct interaction of the active vanadium element with the aqueous electrolyte from the NVO structure during the cycling process and, thus, improves the discharge capacity, cycle life, and rate capability. Another important

observation of this study is the in situ formation of electrolyte by-product MnClO₄·xH₂O·n(OH)_y. In general, the batteries involving aqueous electrolytes are susceptible to promoting proton intercalation in the layered vanadium-based cathodes for ZIBs. Very recently, the succeeding Mn²⁺ and H⁺ (de)intercalation in the layered-type cathode material is reported for MIBs by Bi et al.^[14] It was claimed that the proton insertion is observed as a result of Mn(OH)₂ electrolyte by-product associated with the Mn²⁺ ions in the electrolyte and OH⁻ liberated from the decomposition of water in the electrolyte as H⁺ and OH⁻. To retain the charge balance H⁺ ions in the electrolyte are inserted into the cathode. Likewise, this study witnessed MnClO₄·xH₂O·n(OH)_y as an electrolyte by-product, this might promote H⁺ (de)insertion into the NVO/C cathode as well. In addition, the role of electrolyte by-product MnClO₄·xH₂O·n(OH)_y needs more attention to gain its impact on the capacity and cycle life output of the cathode materials when utilizing MnClO₄·xH₂O as an electrolyte. Moreover, Carbon coating is a well-established technique and demonstrated to improve the cycle life of various batteries including ZIBs and LIBs. Consequently, the carbon coating tactic can be applied to other vanadium-based cathodes, thus providing a way to achieve stable cycle lifetimes in MIBs. The Mn²⁺ ion storage output of NVO/C revealed superior attractiveness in terms of

capacity yield at different current rates and long-term cycling stability outputs (Table S2 and Figure S7).^[13,14,45,46]

Conclusion

Herein, a carbon-coated NaV₆O₁₅ cathode (designated NVO/C) was prepared via a simple wet chemical process, and the influence of carbon coating on the electrochemical Mn²⁺ storage properties was investigated. From the electrochemical outputs, it was established that the ultrathin carbon coating with improved electronic conductivity and interphase durability enhanced the Mn²⁺ storage performance, such that the NVO/C delivered a high rate capability of 65 mAh g⁻¹ at 3.0 A g⁻¹ compared to 52 mAh g⁻¹ for the bare NVO. Further optimization of the carbon coating thickness and amount might promote the practical application of carbon-coated metal-oxide cathodes for MIBs. Moreover, ex-situ XRD and XPS studies demonstrated that the capacity output of the NVO/C cathode is derived from the Mn²⁺ (de)insertion mechanism.

Experimental Section

Synthesis of NVO and NVO/C: To prepare the NVO, sodium acetate (0.54 g; 99%, Sigma Aldrich) was first added to deionized (DI) water (100 mL) and stirred well to obtain a homogeneous solution, designated solution A. Then, vanadium pentoxide (3.63 g; 98%, Sigma Aldrich) was dispersed separately into DI water (50 mL), oxalic acid (5.4 g; 99%, Sigma Aldrich) was added as the reducing agent, and the solution (designated solution B) was mixed well until blueish green. Next, solution B was added to solution A and mixed well for 1 h to attain a homogeneous solution, which was then agitated overnight on a hotplate at 80 °C to obtain a blueish gel. The gel was further dehydrated at 80 °C for 8 h, then annealed at 400 °C for 4 h in air. For the preparation of the NVO/C, NVO (1.0 g) was dispersed in a solution of maleic acid (0.2 g) in ethanol (100 mL) and stirred at 50 °C for 8 h, in accordance with a previously-reported procedure.^[47] After dehydration at 80 °C for 8 h, the product was heated at 350 °C for 3 h under an Argon atmosphere and directly used for further characterization.

Physicochemical properties and other characterizations: Powder X-ray diffraction (PXRD) measurements were performed using a Shimadzu X-ray diffractometer (Cu K_α source, $\lambda = 1.5406 \text{ \AA}$). The morphology and lattice spacings were characterized using field-emission scanning electron microscopy (FE-SEM, Hitachi S-4700) and field-emission transmission electron microscopy (FE-TEM, Philips Tecnai F20, 200 kV; at KBSS Chonnam National University), respectively. Thermogravimetric analysis was carried out using SDT Q600 thermobalance under air atmosphere.

Electrochemical characterization: The as-synthesized cathode material was blended with the conducting carbon super P and a polyacrylic acid binder (450,000, Sigma Aldrich) at a weight ratio of 70:15:15. This blend was then treated with N-methyl-2pyrrolidone (NMP, Sigma Aldrich) to produce a viscous slurry for use as the working electrode. The viscous slurry was then painted smoothly onto stainless-steel foil (SS316, 0.01-mm thickness, MTI Korea) to fabricate the working electrode, which was then dried under vacuum at 80 °C for 8 h. After this, the foil was hot-pressed between stainless steel twin rollers at 120 °C, then cut into ring discs (14 mm). The active mass loading in the disc was found to be in the range of 1.4–1.6 mg. To prepare the reference electrode, a

paste containing active carbon (AC), Ketjen black, and teflonated acetylene black in a weight ratio of 80:10:10 was pushed onto a stainless-steel mesh (16 mm) and vacuum dried overnight at 120 °C. The mass loading of the reference electrode in the stainless-steel mesh was found to be in the range of 8–10 mg. The CR2032 coin-type half cells were then constructed by placing a glass fiber separator between the cathode and AC disc, and 3 M Mn(ClO₄)₂ aqueous solution (150 μL) was employed as the electrolyte. Electrochemical characterization was performed using a multi-channel potentiostat/galvanostat (WBCS 3000/WonATech) with a voltage window of -1.3 to 1.2 V vs. the AC. Specifically, the electrochemical Mn²⁺ storage properties of the NVO/C and the NVO were assessed using the galvanostatic charge/discharge evolution at 0.1 A g⁻¹ in the afore-mentioned electrolyte. To understand the synergistic effect of the carbon coating, the rate capabilities of the materials were measured at current densities of 0.1 to 3.0 A g⁻¹. In addition, cyclic voltammetry (CV) and the galvanostatic intermittent titration technique (GITT) were performed using the Biologic VSP potentiostat model. Specifically, the CV measurements were performed at scan rates of 0.2 to 1.0 mV s⁻¹, and the GITT analysis was performed at 0.2 A g⁻¹ for 10 min, followed by resting for 2 h.

Ex-situ studies: Ex-situ studies were performed on the NVO/C electrodes in the half-cell configuration under 0.1 A g⁻¹ current density. At every cut-off voltage, the cell was maintained under constant voltage mode for 2 h to attain equilibrium. Afterward, the cells were separated in the open atmosphere to recover the electrode for the ex-situ studies, which were then washed with water and dried under a vacuum for 1 day. For the ex-situ XRD analysis, the electrode was directly used after the vacuum drying. Whereas, before the ex-situ XPS studies, the electrodes were etched under argon for 5 min to remove the oxidized product from the surface. Thus, the oxidation exchange of the electrodes during the charge/discharge process was established using X-ray photoelectron spectroscopy (XPS, Thermo VG Scientific Instruments, Multilab 2000) equipped with an Al K_α source. The spectrometer was calibrated using the C 1s peak with a binding energy of 284.6 eV.

Acknowledgements

This work was supported by the National Research Foundation of Korea (NRF) grant funded by the Korea government (MSIT) (NRF-2020R1A2C3012415 and NRF-2018R1A5A1025224). This work was also supported by National Research Foundation of Korea Grant, funded by the Korea Government Ministry of Education and Science Technology (NRF-2021R1I1A3060193). The authors thank Subramanian Nithiananth for his support in XPS studies.

Conflict of Interest

The authors declare no conflict of interest.

Data Availability Statement

The data that support the findings of this study are available from the corresponding author upon reasonable request.

Keywords: carbon coating • manganese-ion batteries • Mn²⁺ intercalation • NaV₆O₁₅/C

- [1] R. Zhang, Z. Wu, Z. Huang, Y. Guo, S. Zhang, Y. Zhao, C. Zhi, *Chin. Chem. Lett.* **2022**, DOI: 10.1016/j.ccllet.2022.06.023.
- [2] B. Sambandam, V. Soundharajan, J. Song, S. Kim, J. Jo, D. T. Pham, S. Kim, V. Mathew, K. H. Kim, Y.-K. Sun, J. Kim, *J. Electroanal. Chem.* **2018**, 810, 34.
- [3] M. Yang, J. Zhu, S. Bi, R. Wang, Z. Niu, *Adv. Mater.* **2022**, 34, 2201744.
- [4] T.-T. Wei, P. Peng, S.-Y. Qi, Y.-R. Zhu, T.-F. Yi, *EnergyChem* **2021**, 57, 169.
- [5] A. Naveed, T. Rasheed, B. Raza, J. Chen, J. Yang, N. Yanna, J. Wang, *Energy Storage Mater.* **2022**, 44, 206.
- [6] Y. Chu, L. Ren, Z. Hu, C. Huang, J. Luo, *Green Energy & Environ.* **2022**, DOI: 10.1016/j.gee.2022.04.008.
- [7] R. Sun, C. Pei, J. Sheng, D. Wang, L. Wu, S. Liu, Q. An, L. Mai, *Energy Storage Mater.* **2018**, 12, 61.
- [8] D. He, D. Wu, J. Gao, X. Wu, X. Zeng, W. Ding, *J. Power Sources* **2015**, 294, 643.
- [9] R. Li, C. Guan, X. Bian, X. Yu, F. Hu, *RSC Adv.* **2020**, 10, 6807.
- [10] Q. Pang, S. Yang, X. Yu, W. He, S. Zhang, Y. Tian, M. Xing, Y. Fu, X. Luo, *J. Alloys Compd.* **2021**, 885, 161008.
- [11] Z. Li, J. Li, F. Kang, *Electrochim. Acta* **2019**, 298, 288.
- [12] Z. Zhu, Y. Meng, Y. Cui, W. Chen, *Adv. Funct. Mater.* **2021**, 31, 2101024.
- [13] S. Bi, S. Wang, F. Yue, Z. Tie, Z. Niu, *Nat. Commun.* **2021**, 12, 6991.
- [14] S. Bi, Y. Zhang, S. Deng, Z. Tie, Z. Niu, *Angew. Chem. Int. Ed.* **2022**, 61, e202200809.
- [15] X. Wu, A. Markir, Y. Xu, C. Zhang, D. P. Leonard, W. Shin, X. Ji, *Adv. Funct. Mater.* **2019**, 29, 1.
- [16] T. Wei, Y. Liu, G. Yang, C. Wang, *Energy Storage Mater.* **2020**, 30, 130.
- [17] J. Zhu, T. Jian, Y. Wu, W. Ma, Y. Lu, L. Sun, F. Meng, B. Wang, F. Cai, J. Gao, G. Li, L. Yang, X. Yan, C. Xu, *Appl. Surf. Sci.* **2021**, 544, 148882.
- [18] H. Qin, L. Chen, L. Wang, X. Chen, Z. Yang, *Electrochim. Acta* **2019**, 306, 307.
- [19] C. Xia, J. Guo, P. Li, X. Zhang, H. N. Alshareef, *Angew. Chem. Int. Ed.* **2018**, 57, 3943.
- [20] T. Wei, Q. Li, G. Yang, C. Wang, *J. Mater. Chem. A* **2018**, 6, 20402.
- [21] V. Mathew, B. Sambandam, S. Kim, S. Kim, S. Park, S. Lee, M. H. Alfaruqi, V. Soundharajan, S. Islam, D. Y. Putro, J.-Y. Hwang, Y.-K. Sun, J. Kim, *ACS Energy Lett.* **2020**, 5, 2376.
- [22] N. Zhang, X. Chen, M. Yu, Z. Niu, F. Cheng, J. Chen, *Chem. Soc. Rev.* **2020**, 49, 4203.
- [23] J. M. Kim, Y. Cho, C. Koo, C. Lee, P. Duenas Ramirez, D. Ko, J. Oh, S. Park, P. Kofinas, S. Begin-Colin, Y. Piao, *J. Electroanal. Chem.* **2021**, 895, 115520.
- [24] W.-M. Zhang, X.-L. Wu, J.-S. Hu, Y.-G. Guo, L.-J. Wan, *Adv. Funct. Mater.* **2008**, 18, 3941.
- [25] S. Islam, M. H. Alfaruqi, B. Sambandam, D. Y. Putro, S. Kim, J. Jo, S. Kim, V. Mathew, J. Kim, *Chem. Commun.* **2019**, 55, 3793.
- [26] H. Liu, Y. Wang, L. Li, K. Wang, E. Hosono, H. Zhou, *J. Mater. Chem.* **2009**, 19, 7885.
- [27] Y. Dong, J. Xu, M. Chen, Y. Guo, G. Zhou, N. Li, S. Zhou, C.-P. Wong, *Nano Energy* **2020**, 68, 104357.
- [28] D. Wu, J. Zeng, H. Hua, J. Wu, Y. Yang, J. Zhao, *Nano Res.* **2020**, 13, 335.
- [29] M. Qin, W. Liu, L. Shan, G. Fang, X. Cao, S. Liang, J. Zhou, *J. Electroanal. Chem.* **2019**, 847, 113246.
- [30] F. Hu, D. Xie, D. Zhao, G. Song, K. Zhu, *J. Energy Chem.* **2019**, 38, 185.
- [31] Q. Wang, S. Wang, J. Li, L. Ruan, N. Wei, L. Huang, Z. Dong, Q. Cheng, Y. Xiong, W. Zeng, *Adv. Electron. Mater.* **2020**, 6, 2000388.
- [32] X. Li, L. Ma, Y. Zhao, Q. Yang, D. Wang, Z. Huang, G. Liang, F. Mo, Z. Liu, C. Zhi, *Mater. Today Energy* **2019**, 14, 100361.
- [33] Y. Li, Y. Liu, J. Chen, Q. Zheng, Y. Huo, F. Xie, D. Lin, *Chem. Eng. J.* **2022**, 448, 137681.
- [34] S. Kim, V. Soundharajan, S. Kim, B. Sambandam, V. Mathew, J.-Y. Hwang, J. Kim, *Nanomaterials* **2021**, 11, DOI: 10.3390/nano11081905.
- [35] J. Jo, S. Nam, S. Han, V. Mathew, M. H. Alfaruqi, D. T. Pham, S. Kim, S. Park, S. Park, J. Kim, *RSC Adv.* **2019**, 9, 24030.
- [36] B. Sambandam, V. Soundharajan, S. Kim, M. H. Alfaruqi, J. Jo, S. Kim, V. Mathew, Y. Sun, J. Kim, *J. Mater. Chem. A* **2018**, 6, 3850.
- [37] B. Sambandam, V. Soundharajan, S. Kim, M. H. Alfaruqi, J. Jo, S. Kim, V. Mathew, Y. Sun, J. Kim, *J. Mater. Chem. A* **2018**, 6, 15530.
- [38] D. Yu, A. Kumar, T. A. Nguyen, M. T. Nazir, G. Yasin, *ACS Sustainable Chem. Eng.* **2020**, 8, 13769.
- [39] L. Chai, X. Wang, Y. Hu, X. Li, S. Huang, J. Pan, J. Qian, X. Sun, *Adv. Sci.* **2022**, 9, 2105063.
- [40] D. Chao, C. Zhu, P. Yang, X. Xia, J. Liu, J. Wang, X. Fan, S. V. Savilov, J. Lin, H. J. Fan, Z. X. Shen, *Nat. Commun.* **2016**, 7, 12122.
- [41] W. Li, K. Wang, S. Cheng, K. Jiang, *Adv. Energy Mater.* **2019**, 9, 1900993.
- [42] N. H. Kwon, H. Yin, T. Vavrova, J. H.-W. Lim, U. Steiner, B. Grobety, K. M. Fromm, *J. Power Sources* **2017**, 342, 231.
- [43] A. Nickol, T. Schied, C. Heubner, M. Schneider, A. Michaelis, M. Bobeth, G. Cuniberti, *J. Electrochem. Soc.* **2020**, 167, 090546.
- [44] V. Soundharajan, B. Sambandam, S. Kim, M. H. Alfaruqi, D. Y. Putro, J. Jo, S. Kim, V. Mathew, Y.-K. Sun, J. Kim, *Nano Lett.* **2018**, 18, 2402, DOI: 10.1021/acs.nanolett.7b05403.
- [45] M. Xie, S. Kong, L. Su, *ChemElectroChem* **2022**, 9, e202101529.
- [46] Q. Yang, X. Qu, H. Cui, X. He, Y. Shao, Y. Zhang, X. Guo, A. Chen, Z. Chen, R. Zhang, D. Kong, Z. Shi, J. Liu, J. Qiu, C. Zhi, *Angew. Chem. Int. Ed.* **2022**, 61, e202206471.
- [47] S. Islam, M. H. Alfaruqi, J. Song, S. Kim, D. T. Pham, J. Jo, S. Kim, V. Mathew, J. P. Baboo, Z. Xiu, J. Kim, *EnergyChem* **2017**, 26, 815.

Manuscript received: December 5, 2022

Revised manuscript received: January 19, 2023

Accepted manuscript online: January 25, 2023

Version of record online: February 7, 2023